Research paper

Hierarchically nanostructured nitrogen-doped porous carbon multi-layer confining Fe particles for high performance hydrogen evolution

Ying Wang [a, 1], Li Jin [a, b, c, d, e, 1], Shiyang Hua [g, 1], Zhe Zhao [b, c, d, e, **], Zhijia Xiao [b, c, d, e], Chunyan Qu [b, c, d, e], Jiayuan Huang [b, c, d, e], Gaoshan Huang [b, d, e, *], Xinyi Ke [b, c, d, e], Zihan Lu [b, c, d, e], Ji Tan [f], Xuanyong Liu [f], Yongfeng Mei [b, c, d, e]

[a] College of Mathematics and Physics, Shanghai University of Electric Power, Shanghai, 200090, China
[b] Department of Materials Science & State Key Laboratory of Molecular Engineering of Polymers, Fudan University, Shanghai, 200438, China
[c] Shanghai Frontiers Science Research Base of Intelligent Optoelectronics and Perception, Institute of Optoelectronics, Fudan University, Shanghai, 200438, China
[d] International Institute of Intelligent Nanorobots and Nanosystems, Fudan University, Shanghai, 200438, China
[e] Yiwu Research Institute of Fudan University, Yiwu, 322000, Zhejiang, China
[f] State Key Laboratory of High Performance Ceramics and Superfine Microstructure, Shanghai Institute of Ceramics, Chinese Academy of Sciences, Shanghai, 200050, China
[g] Wuhan Institute of Marine Electric Propulsion, Wuhan, 430064, China

ARTICLE INFO

ABSTRACT

Precise assembly of active component with sophisticated confinement in electrocatalyst are promising to increase the active site exposure for enhanced hydrogen evolution reaction (HER). Here, PCN-333 films with mesopores are firstly assembled on titanium carbide MXene with the assistance of atomic layer deposited oxide nanomembrane. With the whereafter pyrolysis process, the composite is converted to N-doped porous carbon multi-layer containing Fe nanoparticles. The strong confinement of Fe active particle in carbon as well as great contact between metal and carbon effectively enhance active site exposure. Furthermore, this multi-layer porous structure provides high specific surface area and plentiful mesopores for electrolyte penetration. Due to the structural advantage, the composite can be well functioned in both acid and alkaline electrolytes with excellent HER performance, *e.g.*, low overpotential/Tafel slope. The present work may have great potential in developing high efficiency transition-metal based electrocatalysts.

1. Introduction

With the rapid development of society, the energy issue has received increasing attention. Owing to the unsustainability of fossil fuels and limitations of wind, tide, and solar energy, hydrogen energy has become one of the most promising technologies due to its high heating value and environmental friendliness [1].

Electrochemical water splitting provides a green and sustainable way for hydrogen fuel production. However, Hydrogen evolution reaction (HER) and oxygen evolution reaction (OER) at the cathode and anode, respectively are thermodynamically uphill [2,3], and therefore, highly active electrocatalysts are required to increase the reaction rate and reduce the overpotential in the HER process [4,5]. Noble metals like platinum have been proved as benchmarking catalysts for HER [6,7]. Nevertheless, the high price and rareness of Pt resources hamper the widespread application. Thus, it is necessary to prepare superior performance and cost-effective non-noble metal electrocatalysts for practical HER. So far, a huge variety of materials/structures with large specific surface areas [8], extremely active sites [9,10], or doped nonprecious transition metals [11–15] have been explored. For instance, Shui *et al.* reported phosphated IrMo bimetallic cluster supported by macroporous nitrogen-doped carbon (IrMoP/MNC) as a highly efficient

* Corresponding author. Department of Materials Science & State Key Laboratory of Molecular Engineering of Polymers, Fudan University, Shanghai, 200438, China.
** Corresponding author. Department of Materials Science & State Key Laboratory of Molecular Engineering of Polymers, Fudan University, Shanghai, 200438, China.
  E-mail addresses: zzhao@fudan.edu.cn (Z. Zhao), gshuang@fudan.edu.cn (G. Huang).
  Peer review under responsibility of The Chinese Ceramic Society.
[1] Y. Wang, L. Jin, and S. Y. Hua contributed equally to this work.

alkaline HER catalyst, and excellent catalytic performance is achieved [16]. In addition, Wu *et al.* [17] reported an ultralow Pt-decorated hierarchical Ni−Mo porous hybrid, consisting of Ni$_3$Mo$_3$N on MoO$_2$ microcolumns, which is applicable to all-pH HER with remarkable performances. From viewpoint of the practical applications, it is significant to constantly develop electrocatalysts with high performance [18,19].

Metal organic frameworks (MOFs) are a series of porous materials composed of metal ions and organic ligands [19]. Due to the extremely large surface area, porous structure and good thermal stability, MOFs-based materials have been considered as ideal materials for catalysis applications [20]. However, MOFs-based structures still face several challenges when being applied to HER [21]. First, the narrow pore size distributions with insufficient surface area and the lack of mesopores hinder the penetration of electrolyte in the electrode. Second, severe aggregation or random distribution of MOFs particles and active components reduces the catalytic efficiency. Third, poor contact between carbon and active metal nanoparticles may hinder the ion transportation in term of large resistivity. Forth, low dimensional composite structure leads to poor active site exposure [19]. Consequently, traditional MOFs based composites exhibit unsatisfied electrochemical catalytic performance. To solve these issues, fabricating MOFs-based composite to confine the active metal nanoparticle in the hierarchically porous structures which is highly conductive might be a strategy. In order to avoid the aggregation of MOFs particles, integration of particles on substrate could be a solution as the adhesion between particles and substrate should keep the particles from aggregation. However, approaches applied to uniformly integrate MOFs particles onto substrates are fairly limited [22]. Recently, we developed an efficient method *via* utilizing oxide nanomembrane which is produced by atomic layer deposition (ALD). A uniform MOFs film is then grown onto the complex micro/nano substrates with the induction effect of the oxide nanomembrane [19,23−27]. The strong adhesion force between the MOFs film and the substrate material brings about the composites with excellent structural stability. Specifically, growth of MOFs film on sophisticated 3D substrate produces large ion-accessible surface to shorten dramatically the diffusion distance of ion transportation [19] and sufficient redox active sites exposure can be realized due to the retained large surface area.

For the selection of suitable MOFs material, we noticed that PCN-333 with mesoporous structure and high contents of Fe and N components is a good alternative for design and fabrication of electrocatalyst [28,29]. Moreover, PCN-333 carbonized at high temperature can produce unique porous carbon layer confining Fe particles due to high content of Fe−N component. Meanwhile, the preserved functional active sites could be uniformly embedded into the skeleton [30]. In order to bring PCN-333's superiority into full play, herein, a 2D titanium carbide (Ti$_3$C$_2$T$_x$) MXene is used as an active supporter for PCN-333 film. The MXene is chosen as substrate mainly due to its excellent electronic conductivity and unique layered structure consisting of conductive transition metal carbides [31−33]. Specifically, the unique accordion-like structure of the MXene can provide a huge specific surface area for growth of PCN-333 film and avoid aggregation of MOFs particles. The excellent electrical conductivity can make up for the deficiency of PCN-333 film. Then, PCN-333 films are precise assembled conformally on the surface of inter-connective MXene sheet by an ALD-oxide nanomembrane induction strategy [19]. During the pyrolysis process, PCN-333 layer is transferred into porous carbon layer confining Fe spherical particles, which shows large surface area and high porosity. Due to the strong adhesion between PCN-333 layer and Mxene sheets in current fabrication approach, Fe nanoparticles are effectively embedded in the porous carbon multiple sheets,

forming Fe, N co-doped hierarchically layered porous carbon structure (Fe−N-HLPCS). In alkaline electrolyte, Fe−N-HLPCS exhibits a low overpotential and a low Tafel slope, and the performance still remains well in acid electrolyte, indicating the universality of Fe−N-HLPCS electrocatalyst. Density functional theory (DFT) calculation specifically reveals that the coordination interaction of porous layer consisting of spherical Fe particles alters the electronic structure of the MXene support to achieve an optimal value of Gibbs hydrogen adsorption free energy, which favorably enhances HER performance. We have faith in that the findings of this study can generate new ideas for the rational design of highly efficient catalysts at nanoscale.

2. Experimental section

2.1. Sample preparation

Materials: Ti$_3$AlC$_2$, hydrofluoric Acid (HF), N−N-Dimethylformamide (DMF), nafion (5%, in mass), and iron chloride solution (FeCl$_3$) were purchased from Aladdin Ltd. (Shanghai, China). Pt/C catalyst was obtained from Alfa Aesar and was used as reference for comparison. 4,4′,4″-s-Triazine-2,4,6-triyl-tribenzoic acid (H$_3$TATB, 95%) was purchased from Sigma-Aldrich. None of the reagents has been further purified. All the deionized (DI) water applied in this experiment is purified from a Millipore system.

Fabrication of Ti$_3$C$_2$T$_x$: With reference to published literature [31], a total of 0.5 g of Ti$_3$AlC$_2$ powder was added slowly to 10 mL 10% (in mass) HF solution and the mixture is stirred with the help of a Teflon magnetic bar. The reaction was then allowed to proceed at room temperature (~23 °C) for 24 h. The resulting precipitate was washed separately five times *via* centrifugation (3,500 r/min). The washing cycles were repeated until the pH of the supernatant became ~6.

Fabrication of ZnO nanomembrane: ZnO nanomembrane on MXene (*i.e.*, MXene (ALD)) is prepared through ALD. In a homemade reactor, ZnO nanomembrane is deposited on the surface of MXene at 150 °C. Diethylzinc (DEZ) and DI water are precursors, and one ALD cycle is performed by 40 ms DEZ pulse, 10 s waiting time, 30 s N$_2$ purge, 40 ms DI water pulse, 10 s waiting time, and 30 s N$_2$ purge. In our work, 300 ALD cycles were used unless individually specified.

Induced growth of PCN-333 on MXene: FeCl$_3$ (0.3 g) was dissolved in the 50 mL dimethyl formamide (DMF) to form solution A. 2,4,6-Tris(4-carboxyphenyl)-1,3,5-triazine (0.25 g) was dissolved in the DMF to form solution B. The MXene substrate was placed into a beaker which contained solution A, and then the beaker was sealed at 150 °C in the oven for 24 h. After cooling to the room temperature, solution B was slowly added. Then the beaker was sealed again and placed into the oven under 150 °C for 24 h. Finally, the sample was taken out from the beaker and washed with ethanol. The produced sample was called PCN-333/MXene and subsequently dried at 60 °C.

Fabrication of the Fe−N-HLPCS composites: The produced PCN-333/MXene was heated at high temperature (typically 800 °C) in the tube furnace, with 5 °C/min heating rate and holding for 2 h.

Synthesis of the PCN-333 powder: PCN-333 powder was also produced for comparison. Solution A and solution B were mixed slowly, and then the beaker was sealed in the oven at 150 °C. After 24 h, the sediment was centrifuged out and washed by ethanol. Finally, the sample was dried at 60 °C.

Growth of PCN-333 on Ni foam: ZnO nanomembrane was deposited on Ni foam by ALD. The sample was then placed into a beaker containing solution A. solution B was added and the mixture was sealed at 150 °C for 24 h to growth PCN-333 layer. After cooling down to room temperature, the sample (named as PCN-333/Ni

foam) was subsequently washed with ethanol for three times and dried at 60 °C for 12 h in vacuum.

2.2. Structural and compositional characterizations

Morphologies of the samples were characterized by scanning electronic microscopy (SEM, VEGA TS 5136 MM, TESCAN) and transmission electron microscopy (TEM, Tecnai G2 20 TWIN). The composition of the sample was analyzed during the TEM characterization process by using Energy dispersive X-ray (EDX, Oxford XMax 80T) spectroscopy. The X-ray diffraction (XRD) patterns were obtained by an X'Pert Pro X-ray diffractometer equipped with Cu K$_{\alpha}$ radiation (0.154 2 nm) with a 40 mA current and a 40 kV voltage. A Quantachrome Instruments was applied to perform the nitrogen sorption/desorption experiment. The multi-point BET approach was used to calculate the specific surface area. The nitrogen sorption data was applied to calculate pore size distributions *via* the nonlocal density functional theory (NLDFT) which is provided by the software ASiQwin. Thermal gravity analyses (TGA) were performed by an STA449F3 instrument (NETZSCH, Germany) in the N$_2$ atmosphere with heating rate (10 °C/min). X-ray photoelectron spectroscopy (XPS) analyses were measured by a VG ESCALAB 220I-XL device. The analyses of the XPS curves were accomplished by XPS Peak 4.1 software.

2.3. Electrochemical characterizations

The electrochemical HER tests were evaluated on a CHI 660E (CH Instrument, Shanghai, China) with three-electrode configuration and performed in different electrolytes (*e.g.*, 1 mol/L KOH and 0.5 mol/L H$_2$SO$_4$). During the experiment, we used Ag/AgCl which was saturated in KCl solution as a reference electrode. Meanwhile graphite rod was adopted as a counter electrode. The powder-like samples were pasted on glassy carbon by using nafion to prepare the working electrode. EIS characterizations were executed in certain frequency range (10^5–0.01 Hz). More experimental details were placed in the Support Information.

2.4. DFT calculation

First-principles calculations were carried out on the basis of periodic DFT by using a generalized gradient approximation within the Perdew-Burke-Ernzerhof exchange correction function. The wave functions were constructed from the expansion of plane waves with an energy cutoff of 450 eV. Gamma centered *k*-point of $3 \times 3 \times 1$ have been used for geometry optimization. The consistence tolerances for the geometry optimization were set as 1.0×10^{-5} eV/atom for total energy and 0.05 eV/Å for force. In order to avoid the interaction between the two surfaces, a large vacuum gap of 15 Å has been selected in the periodically repeated slabs. We adopted the projector-augmented wave method for describing ionic cores as implemented in Vienna abinitio simulation package (VASP).

3. Results and discussion

MXene as a substrate is prepared from MAX phase (M: transition metal, A: main group element, X: C and/or N) Ti$_3$AlC$_2$. The Al layers were selectively removed by hydrofluoric acid (HF) and thereby few-layered Ti$_3$C$_2$T$_x$ MXene could be produced [34]. As shown in the (Fig. S1), MAX phase exhibits a bulk structure, while MXene shows a muti-layered structure (Fig. S2). A schematic representing the synthesis of the Fe−N-HLPCS catalyst is depicted in Fig. 1(a). In this process, MXene surface is firstly coated with uniformly dense ZnO nanomembrane by using ALD (*i.e.*, MXene (ALD)

in Fig. 1(a)). No obvious morphology changes can be seen before and after ALD process due to the dense and conformal coating. Then, PCN-333 film is uniformly grown on it through a liquid phase reaction (*i.e.*, PCN-333/MXene in Fig. 1(a)). The SEM image of PCN-333/MXene reveals the homogeneity of the MOFs component. It should be noted that the morphology of PCN-333 particles prepared *via* conventional solution-based process (Fig. S3) exhibit polyhedron morphology, which is different from current PCN-333 film. This difference is explained as that the particles are grown without confinement while the substrate effectively influences the growth behavior in the case of film. Then, Fe−N-HLPCS is obtained by pyrolysis of the PCN-333/MXene under N$_2$ flow at high temperature (typically, 800 °C) for 2 h, leading to the formation of hierarchically layered structure (Fe-HLPCS in Fig. 1(a)). Specifically, during the carbonization process, PCN-333 particles shrunk slightly in particle size and Fe ions were reduced to Fe nanoparticles. It should be noted the morphology of PCN-333 derived carbon particles in the film exhibit a sphere morphology which is inconsistent with conventional carbonized PCN-333 (C−PCN-333) particles (Fig. S4), because the strong adhering between MOFs and MXene hindered the volume shrinkage of MOFs during the carbonization process. We used TEM and EDX to further record the microstructural property of prepared samples. From Fig. 1(b), it can be seen that Fe nanoparticles exist and are distributed uniformly in the sample, and no aggregation can be seen in high-resolution TEM (HRTEM) image (Fig. 1(c)), confirming the embedding of Fe nanoparticles with an average size of 50 nm in carbon matrix. It should be noted that smaller sphere size of active transition metal can enhance the active site exposure thereby enhancing the catalytic property [34]. The EDX mapping of Fe is shown in Fig. 1(d), while the distributions of C, O, Ti, and N elements are showed in Fig. S5. The results strongly suggest the homogeneous distribution of isolated Fe nanoparticles in the Fe−N-HLPCS composite. In addition, the PCN-333/MXene is carbonized at a higher temperature (900 and 1,000 °C), and the result is shown in Fig. S6. The lamellar structure does not change significantly, proving the great thermal stability of the sample during the carbonization process.

We have carried out more characterizations to elucidate the structure and composition of the Fe−N-HLPCS. For an in-depth understanding of catalyst, XRD patterns of the samples are shown in Fig. 2(a), S7, and S8. The diffraction peaks of MAX phase (Fig. S7) are aligned with those published in the literature [35], suggesting the successful removal of Al layers. After ZnO nanomembrane of 300 cycles are deposited (plot: MXene (ALD)), the XRD curve exhibits no additional obvious diffraction peaks, which is due to the amorphous feature of ALD ZnO nanomembrane. After MOFs films are assembled, a sharp diffraction peak appears in the small angle range (plot: PCN-333/MXene and corresponding enlarged small angle part in Fig. S8), and the position is identical to those of PCN-333 [24]. During the carbonization process, PCN-333/MXene is converted into Fe−N-HLPCS. The diffraction peak of the PCN-333/MXene disappears, which proves that the structure of PCN-333 changes during the carbonization process. On the other hand, the diffraction peak of α-Fe with body-centered cubic structure appears, indicating the formation of Fe particles during the carbonization process [36].

In order to further investigate the chemical state of Fe−N-HLPCS, XPS was used to investigate the elemental composition and valence states of the composite (Fig. 2(b)). The results confirm that the presence of Fe, N, and C, as shown in the inset of Fig. 2(b). Notably, high-resolution Fe 2*p* spectrum can be deconvoluted into two major peaks at 711.4 eV for Fe 2*p*$_{3/2}$ and 725 eV for Fe 2*p*$_{1/2}$, and shake-up satellites around 719 and 733 eV [24,37]. The presence of Fe indicates that the PCN-333 successfully grows on the MXene. The high-resolution N 1*s* XPS spectrum (Fig. S9) shows peaks at
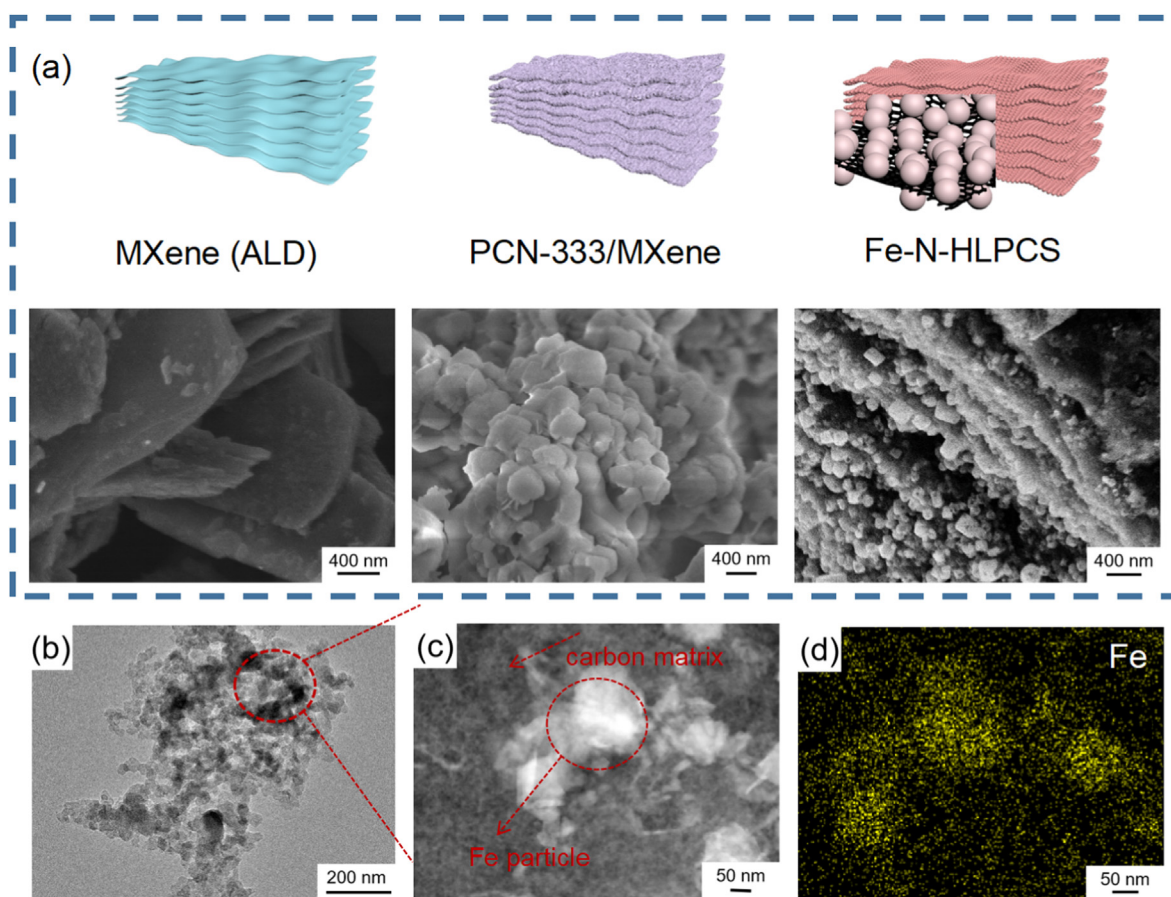
Fig. 1. (a) Schematic illustration of synthetic process of Fe−N−HLPCS. The corresponding images below are SEM images of MXene (ALD), PCN-333/MXene, and Fe−N−HLPCS. (b) TEM image of Fe−N−HLPCS. (c) Enlarged HRTEM image of Fe−N−HLPCS, demonstrating the existence of Fe nanoparticle in the carbon matrix. (d) EDX mapping result of Fe element (corresponding to (c)).

397.2, 400.8 eV, and 403 eV, which are attributed to graphitic nitrogen, pyrrolic nitrogen, and pyridinic nitrogen, respectively, indicating the successful nitrogen doping in the resultant composite [38]. TGA curve of the transition from PCN-333/MXene to Fe−N−HLPCS are shown in Fig. 2(c). Here, the samples were heated up to 800 °C in N_2 atmosphere to probe the phase and morphology changes at a high temperature. One can see that the TGA curve can be divided into two stages. The first stage is from room temperature to ~300 °C, and most of the mass loss occurs in the temperature range of 150−200 °C, due to the loss of physically adsorbed water [39]. The structure of the PCN-333/MXene does not change at this stage. The second stage is from 300 to 800 °C. The high temperature leads to the carbonization of the composite with remarkable mass loss. In addition, the high temperature can break the bonds between terminated groups (*e.g.*, OH/O/F) and PCN-333/MXene [39], which also contributes to the weight loss. The nitrogen adsorption-desorption isotherms and the corresponding pore size distribution are analyzed to further study the porous structure of the prepared composites, and the results are shown in Fig. 2(d). Both PCN-333/MXene and Fe−N−HLPCS show type I and type IV isotherms because of the assembly of particles in the films. It is implied that the porous structure consists of micropores and mesopores, while such porous structure can hardly be detected in pure MXene in Fig. 2(d). Based on NLDFT model, the specific pore size distributions are calculated, and the results are shown in Fig. 2(e). Consistent with isotherms, open mesopores with average size of ~4 nm exist in both PCN-333/MXene and Fe−N−HLPCS, which can effectively

promote electrolyte penetration in electrochemical applications. Also, micropores with an average size of ~1.2 nm can be clearly observed from Fe−N−HLPCS, which is beneficial to the exposure of active sites [19]. The concrete pore structure of Fe−N−HLPCS and PCN-333/MXene compared with pure MXene is summarized Table S1. The MXene provides a negligible specific surface area of 4 m^2/g as determined by Brunauer-Emmett-Teller (BET). After MOFs film is assembled, PCN-333/MXene shows an increased specific surface area of 223 m^2/g. On the other hand, Fe−N−HLPCS exhibits the largest BET surface area of 308 m^2/g. The increase in specific surface area suggests that the composite can provide more active sites [24,40]. This phenomenon is caused by the large MOFs loading which is ascribed to the induced growth process. After the carbonization process, Fe nanoparticles with small diameter are confined in the carbon sheet, introducing additional pores around the Fe nanoparticles, and this leads to a further enhancement of surface area. The highly active material loading and large specific surface area of porous structure of Fe−N−HLPCS composites play a crucial role in improving electrochemical catalytic performance, and we will discuss this in detail in the following paragraphs.

The 3D conductive frame with internal connection has the synergetic effect of high electrochemically active site exposure, making Fe−N−HLPCS promising in HER. The electrocatalytic performance of Fe−N−HLPCS electrode in HER is firstly studied in 1 mol/L KOH. In general, a highly efficient HER catalyst could exhibit a low overpotential under a standard current density (10 mA/cm²). Its low Tafel slope should be comparable to Pt catalyst, and it should
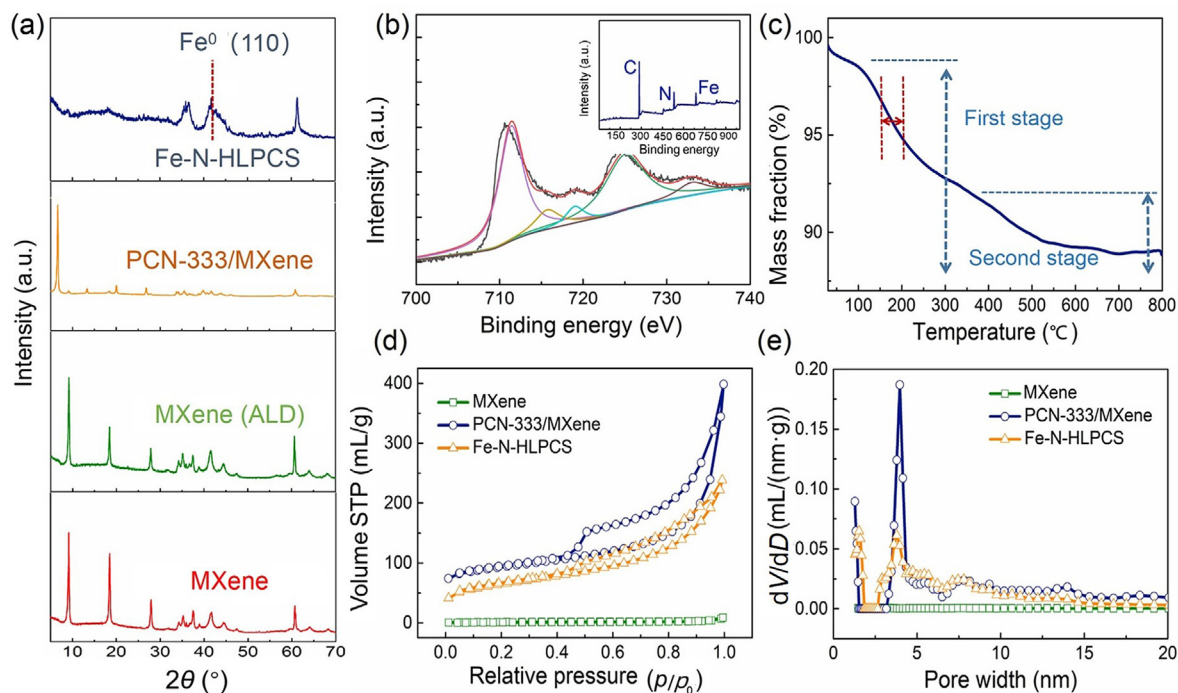
Fig. 2. (a) XRD patterns of the samples. (b) High-resolution XPS spectrum of Fe 2*p*. The inset is the XPS survey scan. (c) TGA curves of Fe−N−HLPCS measured in N_2 atmosphere. (d) Nitrogen adsorption/desorption isotherms. (e) Calculated pore size distributions of MXene, PCN-333/MXene, and Fe−N−HLPCS.

demonstrate excellent durability. The linear sweep voltammetry (LSV) results of samples in 1 mol/L KOH aqueous electrolyte are shown in Fig. 3(a). Taking the Pt/C modified glassy carbon electrode as the benchmark, it showed that at 10 mA/cm² current density the optimal HER catalytic activity and the smallest overpotential were occurred. The PCN-333 powder features large overpotential values of 509 mV, and the LSV curve of PCN-333 powder displays a delayed inflection point in the potential window, demonstrating low electrochemical activity. The deteriorated performance could be mainly caused by the scarce active sites [19]. In addition, the separated individual particles may also hinder the transfer of ions and charges, which have adverse effects on electrochemical performance. Apparently, compared with PCN-333 powder, PCN-333/Ni foam electrodes display strong HER activity and significantly enhanced electrocatalytic performance. The current density can reach 10 mA/cm² at 246 mV, which is much smaller than PCN-333 powder. The results reveal that the PCN-333/Ni foam could effectively enhance the electrocatalytic activity, which is attributed to more active site exposure due to the uniform distribution of MOFs particles in the film. Moreover, PCN-333/MXene shows a lower overpotential (120 mV) compared to PCN-333/Ni foam, and Fe−N−HLPCS electrode shows the highest electrochemical activity (78 mV) in all composite electrodes, which is close to that of the commercial Pt/C (24 mV), as shown in Fig. 3(b). In addition, we also compared the catalytic performance of the Fe−N−HLPCS prepared with different ZnO nanomembrane thicknesses (150 and 300 ALD cycles). The result in Fig. S10 shows that the Fe−N−HLPCS with 300-cycle ZnO nanomembrane exhibits better performance, and thus this sample is engaged for further investigations.

To further investigate the HER kinetics, the Tafel plots were calculated from the linear fitting of the polarization curves, which are shown in Fig. 3(c). Tafel slope of the Fe−N−HLPCS is 55 mV/dec, which is much minor than those of PCN-333/MXene (84 mV/dec) and PCN-333/Ni foam (95 mV/dec). Such a Tafel slope of Fe−N−

HLPCS implies that the Volmer-Heyrovsky joint reaction mechanism dictates the HER process. The electrochemical desorption is a rate-determining process which consists of three main steps (*i.e.*, the Volmer, Heyrovsky, and Tafel). To study the electrochemical surface area (ECSA) and the corresponding catalytic potential active sites, the electrochemical double-layer capacitance (C_{dl}, proportional to ECSA) is measured by cyclic voltammetry (CV) test. The CV results of the prepared samples recorded at various scan rates (Fig. S11) are summarized in Fig. 3(d), and Fe−N−HLPCS possesses the largest C_{dl} of ~1.66 mF/cm², higher than those of PCN-333/MXene (~1.09 mF/cm²), PCN-333/Ni foam (~0.78 mF/cm²), and PCN-333 powder (~0.28 mF/cm²). The highest C_{dl} means more active sites, resulting in excellent electrocatalytic performance in HER application. We also adopted the electrochemical impedance spectroscopy (EIS) to study the catalytic kinetics. Fe−N−HLPCS with steep slopes in the relatively low frequency region (Fig. 3(e) and its inset) indicate minimal charge transfer resistance, that is strongly associated with better electrolyte penetration and faster ion diffusion [41]. We believe that the hierarchically porous structure described above may have contributed to this behavior. Additionally, no obvious semicircles can be observed at high-frequency region, indicating a purely capacitive behavior and low charge-transfer resistances of Fe−N−HLPCS [41]. The high conductivity of Fe−N−HLPCS and carbonized Mxene are further proved by current-voltage (*I*−*V*) curves in Fig. S12, which demonstrates linear relationships and high conductivities are noticed. As a critical characteristic of the catalyst, the cycling performance is probed to investigate the long-term durability of Fe−N−HLPCS, and the data are exhibited in Fig. 3(f). We compare the initial LSV curve of Fe−N−HLPCS with the LSV curve after 2,000 CV cycles. There is only a slight activity loss after 2,000 cycles (*i.e.*, overpotential increases from 78 to 82 mV), proving the good stability of the electrode. To further evaluate the stability of the composite, the LSV curves of PCN-333 powder and PCN-333/MXene before and after 2,000 CV
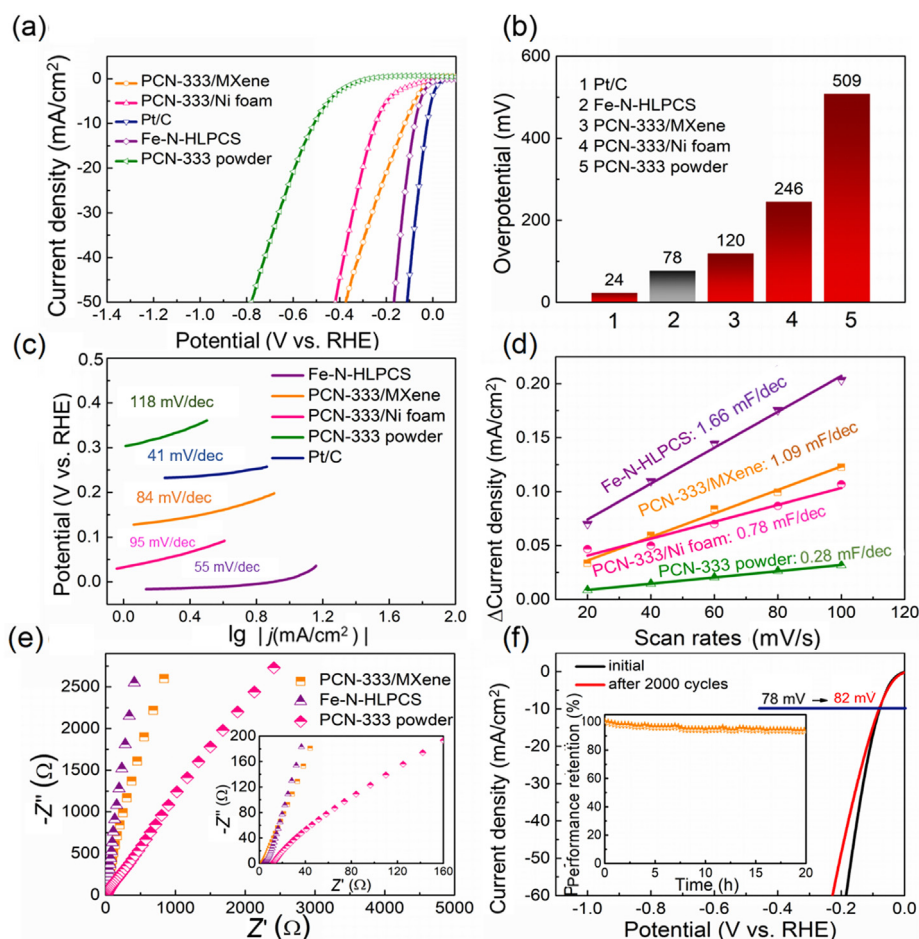
Fig. 3. (a) LSV results of the prepared samples. (b) Comparison of the overpotentials of the samples. (c) Tafel slopes of the samples. (d) C_{dl} result of Fe−N−HLPCS compared with those of PCN-333/MXene, PCN-333/Ni foam, and PCN-333 powder. (e) EIS results of the samples. The inset is the enlarged part of low frequency region. (f) LSV curves of Fe−N−HLPCS before and after 2,000 CV cycles. The inset is the chronopotentiometry durability test of Fe−N−HLPCS in 1 mol/L KOH.

cycles are presented in Figs. S13 and S14. Obviously, these electrodes exhibit poor stability in term of over 80 mV overpotential increment after 2,000 CV cycles. The great structure stability can also be proved by the XRD spectra shown in Fig. S15. Table S2 in supporting information has summarized HER performance of latest MOFs-based composites (in alkaline electrolyte) published in recent literature, and it is worth noting that the present Fe−N−HLPCS exhibits superior HER performance in basic electrolyte. The outstanding electrochemical property can be ascribed to the structural properties of the composite: (i) a large surface area with hierarchically porous structure, (ii) confinement of active metals in carbon which avoids aggregation and leads to good contact therein, and (iii) interconnected multiple layered architecture with high conductivity.

The electrochemical performance of MOFs-based HER catalyst commonly drop dramatically in acidic electrolyte due to the collapse of MOFs structure. Fig. S16 shows the HER performance of PCN-333 powder in electrolytes with various pH values, and it can be noted the electrochemical performance obviously declines with the decrease of pH value. For Fe−N−HLPCS, it is considered that the confinement of the Fe nanoparticles in carbon can protect the composite structure thereby maintaining the electrochemical performance in acidic electrolyte. Here, HER performance of Fe−N−HLPCS is measured in a 0.5 mol/L H$_2$SO$_4$ solution as shown in Fig. 4(a). The carbonized PCN-333 powder (C−PCN-333) and the

commercial Pt/C electrodes are applied as references. To achieve a current density of 10 mA/cm^2, Fe−N−HLPCS shows a lower overpotential (52 mV) than that of C−PCN-333 (584 mV), and Pt/C electrode shows a value of 30 mV. A more intuitive comparison is shown in Fig. 4(b). In addition, Tafel plots calculated according to linear fitting of polarization lines are shown in Fig. 4(c). Tafel slope of Fe−N−HLPCS is 43 mV/dec which is much smaller than that of C−PCN-333 (113 mV/dec). Fig. 4(d) shows the EIS results of C−PCN-333, Fe−N−HLPCS, and Pt/C measured in a 0.5 mol/L H$_2$SO$_4$ solution. Compared to C−PCN-333, Fe−N−HLPCS exhibits much smaller charge transfer resistance, which elucidates that the HER process occurs effectively at the interface between the surface and electrolyte. We should stress that, compared with other similar catalysts, Fe−N−HLPCS shows very good performance in acidic electrolyte (Table S3 in Supporting Information). In addition, the LSV curve of Fe−N−HLPCS was also measured in phosphate buffer solution (pH = 7.4) and the result is shown in Fig. S17. The Fe−N−HLPCS electrode achieves a standard current density of 10 mA/cm^2 at 277 mV, indicating that this electrode could be widely applied in practical applications.

To obtain an understanding of the catalytic nature of Fe−N−HLPCS at the atomic scale, we carried out DFT calculations that provides a basic understanding of improved HER activity of composite. In the calculation, we used the generalized gradient approximation for describing ionic cores as implemented in the
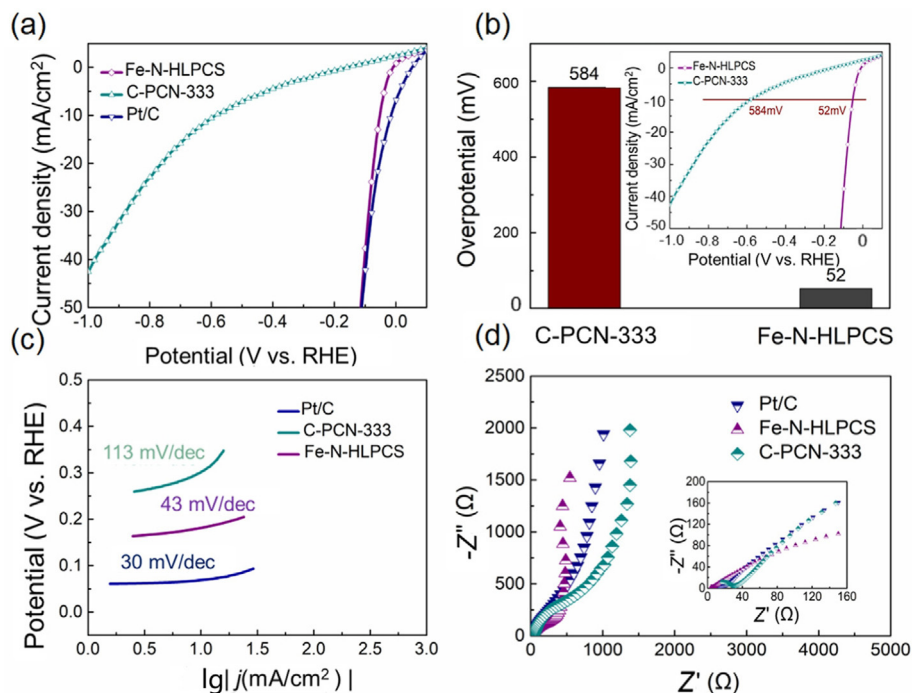
Fig. 4. (a) LSV curves of the samples measured in 0.5 mol/L H_2SO_4. (b) Comparison of overpotentials of C−PCN-333 and Fe−N-HLPCS. The inset shows corresponding LSV curves. (c) Tafel slopes of the samples. (d) EIS results of the samples. The inset is the enlarged part of low frequency region.

VASP. Here, in the HER, H_2O dissociation-adsorption process was considered. Meanwhile, the alkaline HER follows these key steps:

Volmer step: $H_2O + 2e^- + * \rightarrow H* + OH^-$;

Tafel step: $H* + H* \rightarrow H_2$;

Heyrovsky step: $H_2O + H* + e* \rightarrow H_2 + OH^- + *$

As shown in Fig. 5(a), the process is seen spontaneously by the downstairs in the first two steps of the Gibbs free energy curve, so the Heyrvosky is the decisive step of the reaction. We describe the HER reaction process in an alkaline environment as four stages: the initial state, catalytic hydrodissociation, hydrogen ion adsorption,
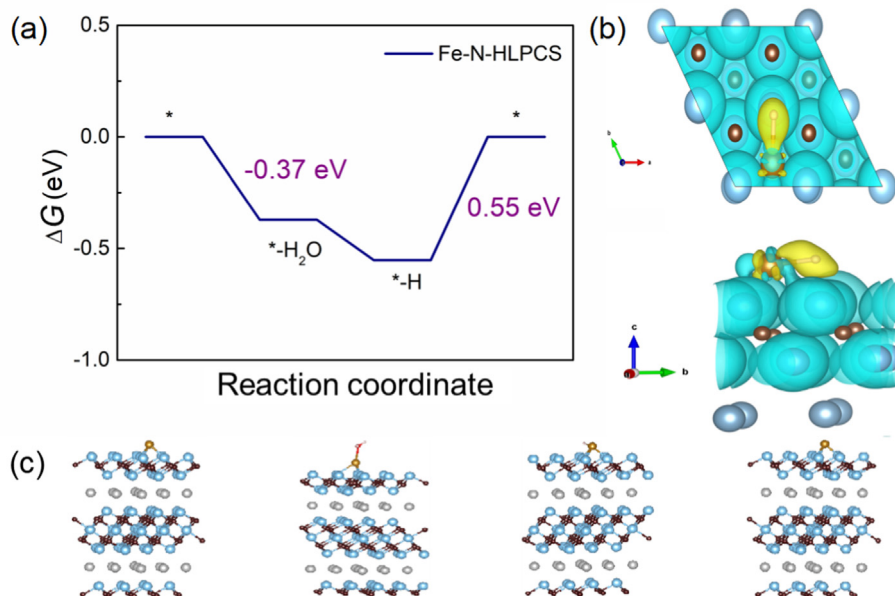

Fig. 5. (a) Calculated free energy distribution in alkaline solution. (b) Structures of estimated intermediate bond to the water and hydrogen (H) atom. (c) Charge density transfer of adsorbed H on the Fe−N-HLPCS.

and hydrogen production. The calculated Gibbs free energy to produce hydrogen is 0.55 eV, which demonstrates a low hydrogen adsorption energy with a small energy barrier which is required for the kinetic process. The theoretical calculation is consistent with the actual experimental results, which reveals the kinetic reasons for the excellent alkaline HER activity of Fe−N-HLPCS from a theoretical perspective. In order to understand the effect of charge transfer on the catalytic activity, the systematic charge transfer is also calculated based on the free energy model (Fig. 5(b)). The whole reaction of composite is visually exhibited in Fig. 5(c). The calculation results show that when Fe atoms are introduced, it effective generates new active sites and reduces the HER over-potential, leading to accelerated electron loss and optimized HER performance of Fe−N-HLPCS.

4. Conclusion

In summary, an efficient Fe−N-HLPCS composite electrocatalyst is constructed by combining ALD ZnO nanomembrane induced growth of PCN-333 film on MXene and following carbonization, and Fe nanoparticles confined in the porous carbon multi-layer are noticed in the composite. The internal connected skeletons with hierarchically porous structure provide large specific surface area, and Fe nanoparticles improve the catalytic performance of Fe−N-HLPCS. The composite can functioned in both acid and alkaline electrolytes with excellent HER performance — overpotential of 78 mV and Tafel slope of 55 mV/dec in 1 mol/L KOH, while in 0.5 mol/L H_2SO_4 electrolytes the values are 52 mV and 43 mV/dec, respectively. Meanwhile, DFT calculation confirms that Fe−N-HLPCS can facilitate H desorption and reduce the kinetic barrier of the HER process to optimize the performance. Our work may pave a new avenue for the design and fabrication of highly active MOFs-based nanoscale electrocatalysts as replacements of precious Pt.

Author contributions

Y. W. and L. J. and S. Y. H. contributed equally to this work. L. J., Z. Z. and G. S. H. conceived the ideas and designed the experiments, analyzed the data, and prepared the manuscript, L. J. performed the chemical synthesis and measurements. All authors contributed to discussion and analyses of the data.

Declaration of competing interest

The authors declare that they have no known competing financial interests or personal relationships that could have appeared to influence the work reported in this paper.

Acknowledgements

Appendix A. Supplementary data

References

[1] Seh ZW, Kibsgaard J, Dickens CF, et al. Combining theory and experiment in electrocatalysis: insights into materials design. Science 2017;355:4998–5009.

[2] Wu YC, Wei W, Yu RH, Xia LX, Hong XF, Zhu JX, et al. Anchoring sub-nano-meter Pt clusters on crumpled paper-like MXene enables high hydrogen evolution mass activity. Adv Funct Mater 2022;32:2110910–7.

[3] Xu HB, Fei B, Cai GH, Ha Y, Liu J, Jia HX, et al. Boronization-induced ultrathin 2D nanosheets with abundant crystalline−amorphous phase boundary supported on nickel foam toward efficient water splitting. Adv Energy Mater 2019;10:1902714–22.

[4] Wu Z, Yang P, Li Q, Xiao W, Li Z, Xu G, et al. Microwave synthesis of Pt clusters on black TiO_2 with abundant oxygen vacancies for efficient acidic electro-catalytic hydrogen evolution. Angew Chem Int Ed 2023;62:e202300406.

[5] Wen Y, Wei Z, Ma C, Xing X, Li Z, Luo D. MXene boosted CoNi-ZIF-67 as highly efficient electrocatalysts for oxygen evolution. Nanomater-Basel 2019;9: 775–85.

[6] Wu Z, Zhao Y, Xiao W, Fu Y, Jia B, Ma T, et al. Metallic-Bonded Pt-Co for atomically dispersed Pt in the Co_4N matrix as an efficient electrocatalyst for hydrogen generation. ACS Nano 2022;16:18038–47.

[7] Li C, Chen Z, Yi H, Cao Y, Du L, Hu Y, et al. Polyvinylpyrrolidone-coordinated single-site platinum catalyst exhibits high activity for hydrogen evolution reaction. Angew Chem Int Ed 2020;59:15902–7.

[8] Lu H, Zhang Y, Huang Y, Zhang C, Liu T. Reaction packaging $CoSe_2$ nano-particles in N-doped carbon polyhedra with bifunctionality for overall water splitting. ACS Appl Mater Interfaces 2019;11:3372–81.

[9] Zhe L, Jian F, Yi F, Cun D, Hui L, Du XW. A silver catalyst activated by stacking faults for the hydrogen evolution reaction. Nat. Catal. 2019;2:1107–14.

[10] Guo H, Feng Q, Xu K, Xu J, Zhu J, Zhang C, et al. Self-templated conversion of metallogel into heterostructured TMP@carbon quasi-aerogels boosting bifunctional electrocatalysis. Adv Funct Mater 2019;29:1903660–71.

[11] Chen Z, Li Q, Xiang H, Wang Y, Yang P, Dai C, et al. Hierarchical porous NiFe-P@NC as an efficient electrocatalyst for alkaline hydrogen production and seawater electrolysis at high current density. Inorg Chem Front 2023;10: 1493–500.

[12] Retuerto M, Pascual L, Vallejo CF, Ferrer Pilar, Gianolio D, et al. Na-doped ruthenium perovskite electrocatalysts with improved oxygen evolution ac-tivity and durability in acidic media. Nat Commun 2019;10:2041–50.

[13] Shen P, Zhou B, Chen Z, Xiao W, Fu Y, Wan J, et al. Ruthenium-doped 3D Cu_2O nanochains as efficient electrocatalyst towards hydrogen evolution and hy-drazine oxidation. Appl Catal B Environ 2023;325:122305.

[14] Gao YX, Chen Z, Zhao Ying, Yu WL, Jiang XL, He MS, et al. Facile synthesis of MoP-Ru_2P on porous N, P co-doped carbon for efficiently electrocatalytic hydrogen evolution reaction in full pH range. Appl Catal B Environ 2022;303: 120879.

[15] Wu ZX, Gao YX, Wang ZX, Xiao WP, Wang XP, Li B, et al. Surface-enriched ultrafine Pt nanoparticles coupled with defective CoP as efficient trifunctional electrocatalyst for overall water splitting and flexible Zn-air battery. J Catal 2023;46:36–47.

[16] Guo X, Wan X, Liu Q, Li Y, Li W, Shui J. Phosphated IrMo bimetallic cluster for efficient hydrogen evolution reaction. eScience 2022;2:304–10.

[17] Yu W, Chen Z, Fu Y, Xiao W, Dong B, Chai Y, et al. Superb all-pH hydrogen evolution performances powered by ultralow Pt-decorated hierarchical Ni-Mo porous microcolumns. Adv Funct Mater 2022;33:2210855.

[18] Ming Z, Ling K, Na L, Ying L, Jian Z, Xian B. Synthesis of MOF-derived nano-structures and their applications as anodes in lithium and sodium ion batte-ries. Chem Rev 2019;388:172–201.

[19] Zhao Z, Zhang ZW, Zhao YT, Liu JR, Liu C, Wang ZJ, et al. Atomic layer depo-sition inducing integration of Co, N codoped carbon sphere on 3D foam with hierarchically porous structures for flexible hydrogen producing device. Adv Funct Mater 2019;29:1906365–74.

[20] Jia G, Zhang W, Fan GZ, Li ZS, Fu DG, Hao WC, et al. Three-dimensional hi-erarchical architectures derived from Surface-mounted metal-organic framework membranes for enhanced electrocatalysis. Angew Chem Int Ed 2017;56:13781–5.

[21] Aiyappa HB, Masa J, Andronescu C, Muhler M, Fischer RA, Schuhmann W. MOFs for electrocatalysis: from serendipity to design strategies. Small Methods 2019;3:1800415–28.

[22] Ting Z, Shen JD, Wang ZS, Liu J, Hu RZ, Ouyang LZ, et al. Regulating lithium nucleation and deposition via MOF-derived Co@C-modified carbon cloth for Stable Li Metal Anode. Adv Funct Mater 2020;30:9159–69.

[23] Zhao Z, Kong Y, Lin XY, Liu C, Liu JR, He YY, et al. Oxide nanomembrane

induced assembly of a functional smart fiber composite with nanoporosity for an ultra-sensitive flexible glucose sensor. J Mater Chem 2020;8:226119—29.

[24] Zhao Z, Kong Y, Huang GS, Liu C, You CY, Xiao ZJ, et al. Area-selective and precise assembly of metal organic framework particles by atomic layer deposition induction and its application for ultra-sensitive dopamine sensor. Nano Today 2022;42:101347—55.

[25] Zhao Z, Kong Y, Liu C, Huang GS, Xiao ZJ, Zhu HQ, et al. Atomic layer deposition-assisted fabrication of 3D Co-doped carbon framework for sensitive enzyme-free lactic acid sensor. Chem Eng J 2021;417:129285—94.

[26] Zhao Z, Kong Y, Zhang ZW, Huang GS, Mei YF. Atomic layer-deposited nanostructures and their applications in energy storage and sensing. J Mater Res 2020;35:701—19.

[27] Kong Y, Zhao Z, Wang YQ, Yang S, Huang GS, Wang Y, et al. Integration of metal organic frameworks on tubular whispering-gallery-mode microcavity with nanoporous wall for CO_2 sensing. ACS Appl Mater Interfaces 2021;13:58104—13.

[28] Feng D, Liu TF, Su J, Bosch M, Wei Z, Wan W, et al. Stable metal-organic frameworks containing single-molecule traps for enzyme encapsulation. Nat Commun 2015;6:5979—86.

[29] Armstrong MR, Arredondo KYY, Liu CY, Stevens JE, Mayhob A, Shan B, et al. UiO-66 mof and poly(vinyl cinnamate) nanofiber composite membranes synthesized by a facile three-stage process. Ind Eng Chem Res 2015;54:12386—92.

[30] Bouwkamp-Wijnoltz AL, Visscher W, Veen J, Boellaard E, Kraan A, Tang S. On active-site heterogeneity in pyrolyzed carbon-supported iron porphyrin catalysts for the electrochemical reduction of oxygen: an in situ mössbauer study. Phys Chem B 2002;106:12993—3002.

[31] Ghidiu M, Lukatskaya MR, Zhao MQ, Gogotsi Y, Barsoum MW. Conductive two-dimensional titanium carbide 'clay' with high volumetric capacitance. Nature 2014;516:78—81.

[32] Long Y, Tao Y, Shang T, Yang H, Sun Z, Chen W, et al. Roles of metal ions in MXene synthesis, processing and applications: a perspective. Adv Sci 2022;9:2200296—320.

[33] Cheng Z, Qiu S, Shuo F, Dan D, Yue L. Single-Atom catalysts for electrochemical water splitting. ACS Energy Lett 2018;3:1713—32.

[34] An W, Jun l, Tao Z. Heterogeneous single-atom catalysis. Nat Rev Chem 2018;2:65—81.

[35] Alhabeb M, Maleski K, Anasori B, Lelyukh P, Clark L, Sin S, et al. Guidelines for synthesis and processing of two-dimensional titanium carbide ($Ti_3C_2T_x$ MXene). Chem Mater 2017;29:7633—44.

[36] Zhao SN, Li JK, Wang R, Cai J, Zang SQ. Electronically and geometrically modified single-atom Fe sites by adjacent Fe nanoparticles for enhanced oxygen reduction. Adv Mater 2022;34:2107291—300.

[37] Long C, Jiang L, Wei T, Yan J, Fan Z. High-performance asymmetric supercapacitors with lithium intercalation reaction using metal oxide-based composites as electrode materials. J Mater Chem 2014;2:16678—86.

[38] Zhao Z, Liu SL, Zhu JX, Xu JS, Li L, Huang ZQ, et al. Hierarchical nanostructures of nitrogen-doped porous carbon polyhedrons confined in carbon nanosheets for high-performance supercapacitors. ACS Appl Mater Interfaces 2018;10:19871—80.

[39] Wu M, Wang B, Hu Q, Wang L, Zhou A. The synthesis process and thermal stability of V2C MXene. Materials 2018;11:112112—22.

[40] Wu ZT, Liu C X, Shang TX, Deng YQ, Wang N, Dong XM, et al. Reassembly of MXene hydrogels into flexible films towards compact and ultrafast supercapacitors. Adv Funct Mater 2021;31:2102874—81.

[41] Chen ZL, Wu RB, Liu Y, Ha Y, Guo YH, Sun DL, et al. Ultrafine Co nanoparticles encapsulated in carbon-nanotubes-grafted graphene sheets as advanced electrocatalysts for the hydrogen evolution reaction. Adv Mater 2018;30:1802011—20.

Dr. Zhe Zhao obtained his Ph. D. degrees at Fudan University in 2021. Now, he is a post-doc researcher in Department of Materials Science at Fudan University. His research interest includes the design and synthesis of nanomaterials, new structural electrode materials for electrocatalysts, energy storage devices, and sensors.

Prof. Gaoshan Huang received his PhD in condensed mater physics at Nanjing University, China in 2007. After graduation, he worked in IFW Dresden, Germany as a guest scientist. Then he moved to IMRE, Singapore as a research engineer. In 2010, he joined the Department of Materials Science, Fudan University, China. Currently, he is a professor of materials science at Fudan University. His research interest is fabrications and characterizations of low-dimensional structures.

Professor Yongfeng Mei received his BS and MS in physics from Nanjing University and PhD in materials physics from City University of Hong Kong. He is a professor in materials physics and chemistry and associated department head in the Department of Materials Science at Fudan University (China). Before that, he worked as a post-doctoral researcher in the Max Planck Institute for Solid State Research (Germany) and then led a research group in the Leibniz Institute for Solid State and Materials Research Dresden (Germany) as a staff scientist. His research interest focuses on the materials development in micro/nanorobotics, flexible electronics/optoelectronics and nanophotonics.